Mode-crossing spectroscopy for photonic waveguide characterization

Cite as: APL Photonics 4, 106107 (2019); https://doi.org/10.1063/1.5099368
Submitted: 09 April 2019 . Accepted: 25 September 2019 . Published Online: 11 October 2019

N. F. Tyndall, T. H. Stievater, D. A. Kozak, M. W. Pruessner, and W. S. Rabinovich

Mode-crossing spectroscopy for photonic waveguide characterization

Cite as: APL Photon. 4, 106107 (2019); doi: 10.1063/1.5099368
Submitted: 9 April 2019 • Accepted: 25 September 2019 •
Published Online: 11 October 2019

N. F. Tyndall,[a] T. H. Stievater, D. A. Kozak, M. W. Pruessner, and W. S. Rabinovich

AFFILIATIONS

Optical Sciences, Naval Research Laboratory, Washington, DC 20375, USA

[a]nathan.tyndall@nrl.navy.mil

ABSTRACT

We report a novel spectroscopic technique to characterize photonic waveguides over more than an octave of wavelength. The technique, called mode-crossing spectroscopy, uses a broadband source and a spectrometer that are coupled to the input and output ends of a series of straight dielectric waveguides via single-mode optical fibers. Measurements of the wavelengths at which multiple modes are degenerate in a single waveguide enable the determination of the refractive index of the core, as well as the waveguide width variation. In addition, mode-dependent losses are reported from 700 nm to 1550 nm using waveguides of varying lengths. The core refractive indices are measured within an error of ±0.5%, waveguide width variation to an accuracy of less than 5 nm, and waveguide propagation losses within an error of ±0.5 dB/cm. Ultrabroadband *in situ* measurements of loss and index over an octave of bandwidth are crucial for the accurate characterization of photonic integrated circuits and devices, especially those based on precision broadband couplers, interferometers, and resonant cavities.

I. INTRODUCTION

An increasing number of optical devices are fabricated in waveguide-based photonic platforms, including silicon-on-oxide (SOI); indium phosphide (InP); and amorphous dielectrics such as silicon nitride (SiN), aluminum oxide (Al_2O_3), and titanium oxide (TiO_2). As the applications for these devices expand beyond data communications and telecommunications in the optical C-band, the underlying waveguides and components require characterization at wavelengths in the visible or near-infrared, and over a range of modes and core/cladding material combinations. Knowing the fundamental material properties, such as absorption and refractive index, is critical for successful device design, but often requires *in situ* characterization to account for process-specific performance. For example, plasma-deposited silicon nitrides for waveguides can have indices that vary by more than 10%.[1] Even material refractive indices and absorption can vary from unpatterned films to waveguides (from strain relaxation or free-carrier trapping, for example). Ultrabroadband characterization is particularly important for chemical or biological sensors, such as Raman or fluorescence sensors, that rely on spectroscopy in photonic integrated circuits.[2–5]

The refractive index of a waveguide can be measured with techniques such as near-field coupling,[6,7] prism coupling,[8] evanescent-field imaging,[9] or Fourier imaging,[10] but these techniques require specific surface-normal off-chip optics and may be better suited for planar films than photonic waveguides. More sophisticated waveguide characterization techniques, such as optical vector network analysis or optical reflectometry, can provide a full amplitude and phase description, but are either not wideband (limited to tens of nanometers by the laser tuning range), require sophisticated, phase-stabilized benchtop equipment, or both. Specific waveguide components, such as ring resonators[11–13] or unbalanced Mach-Zehnder interferometers,[14] can be used with tunable lasers to measure propagation loss and effective index, but the required waveguide coupling and laser source restricts the optical bandwidth, and these devices are better suited for group index determination than effective index. Importantly, all of these techniques are based on tunable laser sources, which cannot equal the bandwidth available with a blackbody source.

In this work, we describe a new, facile, *in situ* measurement technique to characterize the optical properties of photonic waveguides over more than an octave of bandwidth: Mode-crossing spectroscopy (MCS). By coupling white light into multimode waveguides

of varying widths, we show that a simple incoherent source (from a heated tungsten filament) can measure modal interference in a waveguide due to degeneracy of the propagation constants (effective indices) of multiple modes. Core refractive indices are measured to an accuracy of approximately ±0.5%. In addition, the variation of the waveguide width can also be determined with MCS, which is important to quantify phase stability in interferometric photonic devices. Finally, using waveguides with varying lengths, the same source and spectrometer permit ultrabroadband propagation and coupling loss measurements to an accuracy of approximately ±0.5 dB/cm and 2 dB, respectively.

II. WAVEGUIDE MODELING

The waveguides considered here comprise SiN waveguide cores fully etched and surrounded by a SiO_2 cladding. We use finite-element analysis (Comsol Multiphysics) to model the effective index (n_{eff}) of a number of low-order waveguide modes, as a function of wavelength, material index, and SiN width and thickness. Figure 1 shows n_{eff} vs wavelength for the lowest order modes for a 1.2 μm wide and 1.5 μm wide waveguide. The degeneracy between the TE_{10} and TM_{00} modes is shown with orange circles, demonstrating the strong dependence of this modal crossing on waveguide width. It is the measured wavelength of this mode crossing that permits the determination of the effective index for these modes, which can then be used to find the core index using our numerical model. Not shown in this figure are additional higher-order mode crossings, such as TM_{00}/TE_{30}, and TM_{00}/TE_{50}, which are also observed experimentally.

III. EXPERIMENTAL METHODS

The first three samples investigated in this work were fabricated using a deep-UV contact photomask aligner (SUSS MJB4). Each sample comprised a 175 nm thick SiN waveguide layer deposited onto a 5 μm thermal silicon dioxide (SiO_2) layer. For this study, we used samples with either a plasma-enhanced chemical vapor deposition (PECVD) SiN layer or a stoichiometric low-pressure chemical vapor deposition (LPCVD) SiN layer. To provide a comparison between samples with different edge roughness and width variation, two different photoresists were employed to pattern the waveguides: ZEP-520A and ma-N 2400. After patterning, the waveguides were fully etched via a fluorine-based inductively coupled plasma reactive-ion etch (ICP-RIE). Finally, the samples were clad with a 3 μm layer of SiO_2 deposited by PECVD. Sample LZ consisted of LPCVD SiN and was patterned using ZEP-520A; Sample PM consisted of PECVD SiN and was patterned using ma-N 2400, and sample PZ consisted of PECVD SiN and was patterned using ZEP-520A. The waveguides used for this work include simple straight waveguides of varying widths for MCS, as well as "paperclip" structures of various lengths and widths for loss analysis. The samples are cleaved into lengths of 9.6 mm or 4.8 mm to expose facets for edge coupling.

A fourth sample, AP, was fabricated at a photonic integrated circuit foundry (AIM Photonics). The PECVD SiN waveguides are 220 nm thick, 8.5 mm long, fully etched, and surrounded by a PECVD SiO_2 cladding.[1]

Figure 2 depicts the experimental setup. A broadband tungsten-filament light source (Thorlabs SLS201L) was coupled into a polarization-maintaining (PM) single-mode optical fiber, which led to a lensed fiber (Oz Optics TPMJ) with the slow axis aligned parallel to the sample plane. From here, the light was coupled into the test device. At the output of the device, a second lensed fiber collected the light and fed it into a second PM single-mode optical fiber coupled to the input of the spectrometer. Two different spectrometers were employed in this work: a 0.5 m focal length with a liquid-nitrogen cooled, 1024 element linearly arrayed InGaAs detector, and a 0.75 m focal length with a liquid-nitrogen cooled, 1024 × 253 element silicon detector. Both spectrometers employed a 300 groove/mm, 1.3 μm blaze grating and were operated via Princeton Instruments LightField data acquisition software. Optical fibers optimized for the wavelength range associated with the detector were used: Nufern PM980-XP for the InGaAs detector (900 nm–1550 nm) and Nufern PM780-HP for the silicon detector (700 nm–1050 nm).

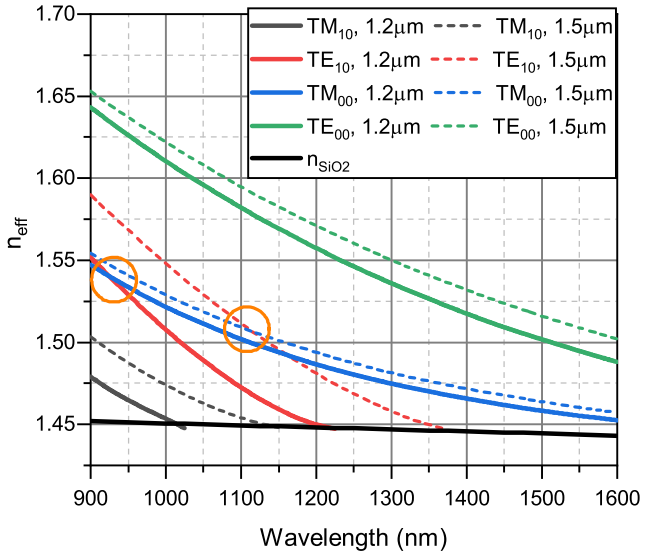

FIG. 1. Simulated n_{eff} vs wavelength for the lowest order modes for a 1.2 μm and a 1.5 μm wide waveguide, along with the SiO_2 material index. The orange circles indicate the wavelength at which the TE_{10} and TM_{00} modes are degenerate.

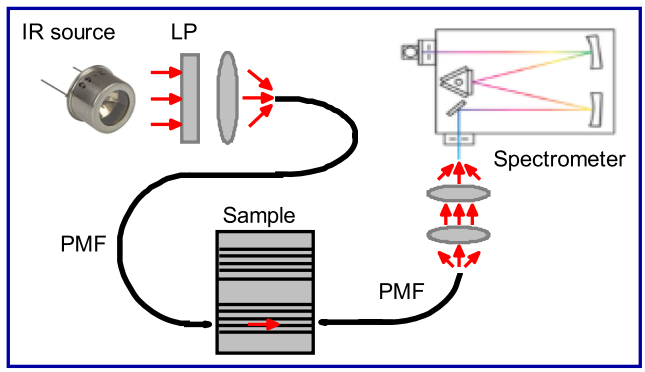

FIG. 2. Experimental set-up. LP: Linear polarizer; PMF: Polarization-maintaining lensed optical fiber.

Sample transmission spectra were acquired in 0.5 s intervals, then normalized to a background spectrum acquired in 0.01 s obtained from connecting the broadband source directly into the spectrometer via a PM fiber. A linear polarizer placed between the broadband source and the input PM fiber provided the ability to send light into the device polarized either parallel to or normal to the sample plane, predominantly exciting the TE_{00} or TM_{00} waveguide mode, respectively.

IV. REFRACTIVE INDEX

Measuring the refractive index of the waveguide core material over a broad wavelength range here requires waveguides of widths varying between 1.0 μm and 3.0 μm, with the wider waveguides required to observe higher-order TE_{30} and TE_{50} modes. Figure 3 plots the normalized TM_{00} waveguide transmission of the four different samples measured with the InGaAs spectrometer. The wavelengths of the transmission minima observed in these spectra depend on the actual waveguide width and the SiN core index.

These minima, which are only observed for excitation polarized normal to the sample plane (exciting the TM_{00} mode), correspond to the wavelengths at which the TM_{00} and TE_{10} modes are degenerate. When both modes possess the same wavevector, they are phase-matched, so small waveguide imperfections can couple the TM_{00} mode into the TE_{10} mode. The lowest-order mode-crossing (TM_{00}/TE_{10}) is observed for the narrowest waveguides, with wider waveguides showing crossings between the TM_{00} mode and successively higher-order odd quasi-TE modes. Since we use lensed optical fibers to collect propagating light via a Gaussian (even) focused spot, any radiation converted to an odd mode will couple more weakly to the lensed fiber than an even mode (such as the TM_{00} mode), thereby showing a transmission minimum. As noted below, the absorption feature near 1385 nm is due to absorption in the cladding of the waveguide and is not related to the mode crossing we have discussed here.

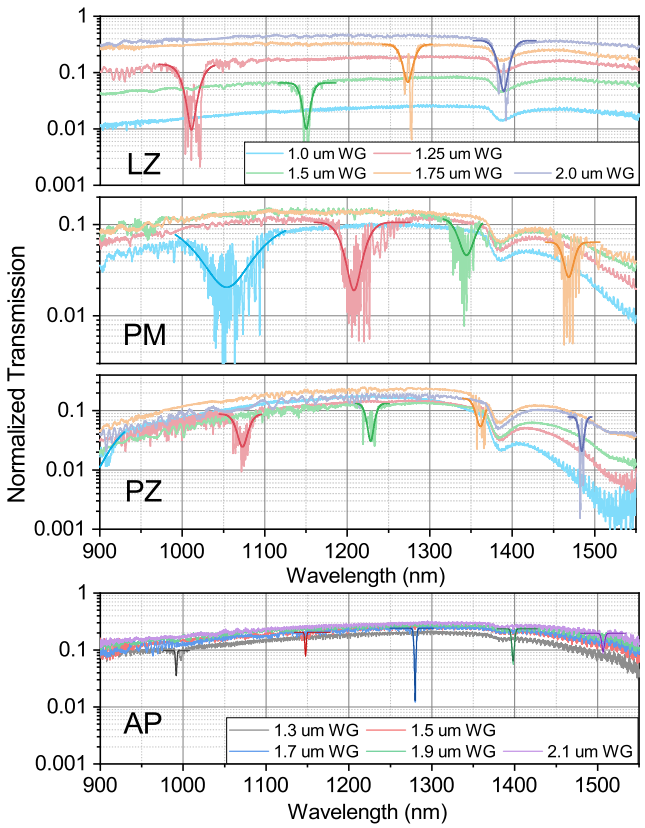

FIG. 3. TM_{00} transmission spectra acquired from straight waveguides of the nominal (photomask) widths for four samples investigated: LZ, PM, PZ, and AP.

The observed short-period oscillation in the measured transmission at wavelengths near the minimum is due to mode-beating between the TE_{00} and TE_{10} modes. The mode-beating period is given by $\lambda^2/(L\,\Delta n_{\text{eff}})$, where L is the length of the waveguide and Δn_{eff} is the effective index difference between the two beating modes. For example, in sample LZ, the calculated period for the TE_{00} and TE_{10} modes at a wavelength of 1150 nm is 2.6 nm, compared to the measured period of 2.2 nm. For sample PM, which is twice as long, the calculated period is 1.4 nm at a wavelength of 1200 nm, compared to the measured period of 1.1 nm. The exact physical origin of the TE_{00}/TE_{10} beating is unclear, but is likely due to the same waveguide imperfections that couple the TM_{00} mode to the TE_{10} mode, such as sidewall roughness. Any power coupled to the TE_{00} mode will couple to our output lensed fiber much more strongly than the TE_{10} mode, since TE_{00} is an even mode.

The waveguide widths reported in Fig. 3 are the nominal (photomask) widths used to fabricated the samples. For the three samples LZ, PM, and PZ, the actual widths of the waveguides varied based on the photoresist and other process parameters used for fabrication. Actual widths and thicknesses of the waveguides in these samples were measured with a scanning electron microscope (SEM) and were offset from nominal widths by amounts ~100 nm.

Since the mode-crossing wavelength for the TE_{x0} and TM_{00} modes depends on the waveguide width and thickness, as well as the refractive indices of the core and cladding, numerical modeling (similar to that shown in Fig. 1) can be used to determine the refractive index of the SiN layer. With the width and thickness measured by SEM, and the SiO_2 index known to relatively high precision,[15,16] the only remaining parameter that determines this mode-crossing wavelength is the SiN index. The transmission minima were fit with a Gaussian function in order to determine the center wavelengths and full-width-half-minimum (FWHM) of the features, and these fits are shown in Fig. 3. The calculated refractive indices from the transmission minima of each sample are reported in Fig. 4. Error bars associated with these points are dominated by the measurement error of the waveguide width (±10 nm) and also contain the contribution of the error in the center wavelength fitting. These error bars imply an index measurement imprecision that is typically smaller than ±0.5%.

As shown in Fig. 4, the refractive indices of samples PM and PZ agree very well, as expected since they were fabricated from the same PECVD SiN. Unfortunately, absorption loss in this material prevents index measurements at wavelengths below approximately 1000 nm.[17] Sample LZ has a significantly lower refractive index, consistent with stoichiometric LPCVD silicon nitride layers. Also

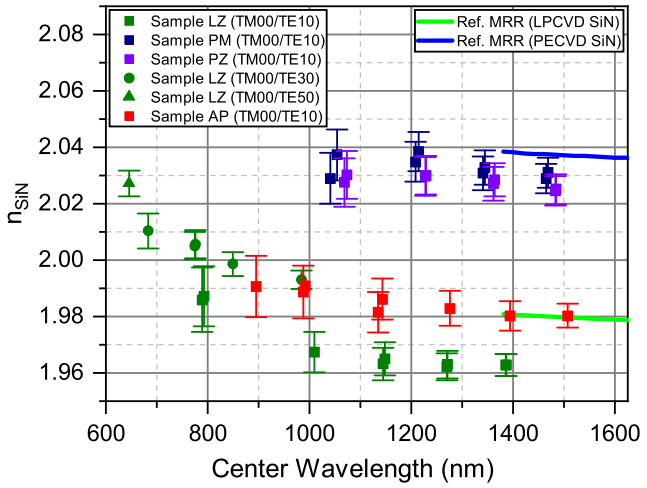

FIG. 4. Values of the SiN core refractive index based on the measured wavelength of the TM_{00}/TE_{x0} mode crossing for the four samples investigated, with x = 1, 3, or 5, as indicated in the caption. Error bars are dominated by uncertainty in the waveguide width. Included for reference are previous measurements of the SiN index deduced from microring resonators.

shown for reference are measurements made previously[12] using tunable lasers coupled to microring resonators, in which the group index and the ring-bus coupling are used to infer the SiN index. The agreement between the two methods is very good, though there is a slight discrepancy between the values for the LPCVD SIN. Figure 4 also shows the inferred SiN index from sample AP, demonstrating the variability of the SiN index within material deposited using a similar (PECVD) method.[1] It is also worth noting that the minima in sample AP are of comparable depth to those of the other samples despite having roughly 10× lower propagation loss, which implies that mode-coupling efficiency does not scale linearly with the amplitude of waveguide imperfections.

V. WAVEGUIDE UNIFORMITY

The fit FWHM value of the transmission minima also have physical significance. Phase-matching between the TE_{10} and TM_{00} modes is characterized by $\mathrm{sinc}^2(\Delta kL)$, where $\Delta k = 2\pi(n_{\mathrm{eff}}^{TE10} - n_{\mathrm{eff}}^{TM00})/\lambda$ and L is the waveguide length. The FWHM of this function (in wavelength) is ~0.2 nm for the waveguides measured here, significantly less than the measured widths of the transmission minima. The measured FWHM thus results from a variation in a physical parameter along the waveguide's length, causing the minima to spread in wavelength. Neither the refractive index nor the thickness of the SiN has enough variation to account for the FWHM, but lithography imperfections resulting in waveguide width variations do. Width nonuniformity is also consistent with the increase in the minima FWHM as the waveguide width is decreased (as shown in Fig. 3).

To calculate the dependence of the mode-crossing bandwidth on the waveguide width, we vary the width of the waveguide in our finite-element model to find $\delta w/\delta\lambda$. Then, the waveguide width variation, Δw, is given by the product of the FWHM and $\delta w/\delta\lambda$.

TABLE I. The variation in the waveguide width as inferred from the FWHM of the TE_{10}/TM_{00} mode crossing.

Sample	LZ	PM	PZ	AP
Δw (nm)	39 ± 10	51 ± 9	23 ± 5	4.6 ± 0.6

The resulting Δw is reported in Table I, along with the standard deviation, as found from the weighted average of these values measured across a number of different waveguides. Samples LZ and PZ, though patterned with the same photoresist, underwent different development processes, which could explain the resulting difference in Δw. These deduced width variations are consistent with our observed lithography nonuniformity in sample PM, as shown by SEM in Fig. 5. As expected, the width variation in the sample fabricated at a photonic integrated circuit foundry (AP) is significantly less than that observed from the samples fabricated using contact photolithography.

While other waveguide imperfections, such as nonvertical sidewalls, could also account for broadening of the TM_{00}/TE_{10} mode crossing, our analysis shows that these contributions are typically negligible compared to width variations. For example, for the waveguides considered here, an angled sidewall would contribute approximately 0.2 nm of minima broadening for every degree of deviation from vertical, compared to our smallest measured FWHM of 2 nm.

Waveguide width nonuniformity is a critical parameter for high-quality photonic fabrication since this width variation results in phase variation through the dependence of n_{eff} on width. The performance of photonic interferometric components, such as phased arrays,[18] or arrayed waveguide gratings depend critically on minimizing this phase nonuniformity. MCS is capable of measuring waveguide width variation, and thus phase nonuniformity, in a simple straight waveguide co-fabricated with the photonic devices of interest. Other techniques, such as optical vector network analysis, can measure the net accumulated phase of a given waveguide, but not its phase velocity variation. It is also important to note that while

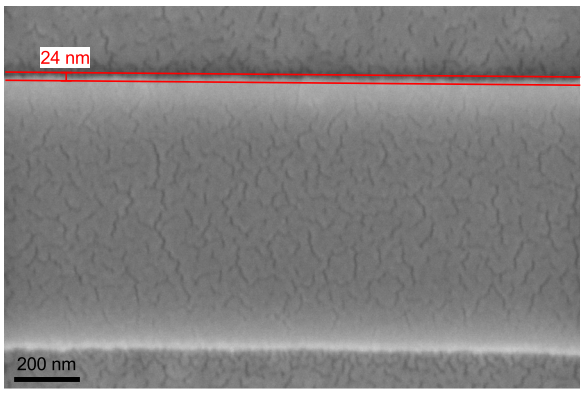

FIG. 5. Top-down scanning-electron micrograph (SEM) of an unclad test structure patterned with the same process as that used for sample PM, coated with ~5 nm of metal for contrast, showing a total width variation of approximately 48 nm.

the waveguide width nonuniformity reported here is likely correlated with sidewall roughness, the exact relationship between these quantities is a subject of further investigation.

VI. LOSS AND DEVICE CHARACTERIZATION

Broadband light coupled into waveguides and measured with a spectrometer also enables straightforward loss measurements. In samples LZ, PM, and PZ, the insertion loss is found by interrogating "paperclip" devices of various lengths with light linearly polarized to excite either the TE_{00} or TM_{00} mode. These paperclips consist of s-bends that looped back and forth over the length of the device in order to vary the waveguiding length in a single die with identical facets. The bend radius in these structures was sufficiently large so that bend losses are negligible compared to propagation loss. Normalized transmission data from waveguides of a single width and varying lengths clearly show the gradual increase in loss as the length of the waveguide increases from 9.6 mm to 29.2 mm.

To separate the propagation loss from the coupling loss for a given waveguide width and polarization, an automated linear fit routine was used to find the slope and intercept of the data as a function of wavelength, corresponding to the propagation and coupling loss, respectively. Figure 6 shows the result of this procedure for a set of 1.5 μm wide waveguides. The error bars correspond to the standard error in the intercept and slope from the fit. We perform this process for each set of devices, for both polarizations, and for multiple widths in each sample. The coupling loss shown here corresponds to total coupling loss—that is, input *and* output coupling. The lowest propagation loss measurable with this technique (here 0.5 dB/cm) is limited by the length of the longest fabricated waveguides (here 29 mm), such that loss in high-quality samples (e.g., <0.1 dB/cm) could be measured with commensurately longer waveguides (e.g., >100 mm).

A comparison of propagation loss for different polarizations, wavelengths, and waveguide widths helps to identify the physical origin of the loss. For example, the loss peak at 1385 nm (assigned to –OH overtone absorption[19]) is more pronounced for the TM_{00} mode than the TE_{00} mode, so it likely originates from the SiO_2 cladding. Since thermal SiO_2 tends to be of higher purity than PECVD-deposited SiO_2, this feature is likely from the top cladding.

The TE_{00} loss spectrum also shows an additional loss peak at 1520 nm that corresponds to an overtone of the Si-H absorption.[20] The near-absence of this peak in the TM_{00} spectrum implies that this absorption is in the SiN layer, as most of the electric field of this mode resides outside of the SiN core. Another notable feature of these spectra is the presence of the cutoff wavelength, observed as a reduction in loss noise for wavelengths above approximately 1200 nm and 1400 nm for the TM_{00} and TE_{00} modes, respectively. These measured cutoffs agree with the calculated wavelengths (see Fig. 1) where the TM_{10} and TE_{10} effective index crosses below the cladding index (that is, where those modes are cutoff).

The coupling loss is relatively flat as a function of wavelength for both polarizations, with an increase of a few dB at lower wavelengths. For comparison, we have included the results of a numerical edge coupling calculation based on the modal overlap of the waveguide mode with that of the Gaussian spot of the lensed optical fiber. The dashed blue and green lines correspond to these theoretical results for the TE_{00} and TM_{00} modes, respectively. Characterizing waveguide couplers over a wide wavelength range is particularly important for low-loss inverse-taper edge couplers, which have been shown to have 3-dB bandwidths of hundreds of nanometers.[21]

Determining physical properties of materials is not the only use of this spectroscopic technique. Broadband characterization of integrated photonic devices is also possible. Even though the bandwidth of our source spans hundreds of nanometers, corresponding to a coherence length of order λ, we can nevertheless accurately measure interferometric devices with differential path lengths of millimeters or longer. This is possible because the spectrometer effectively limits the bandwidth to that of a single pixel, in our case

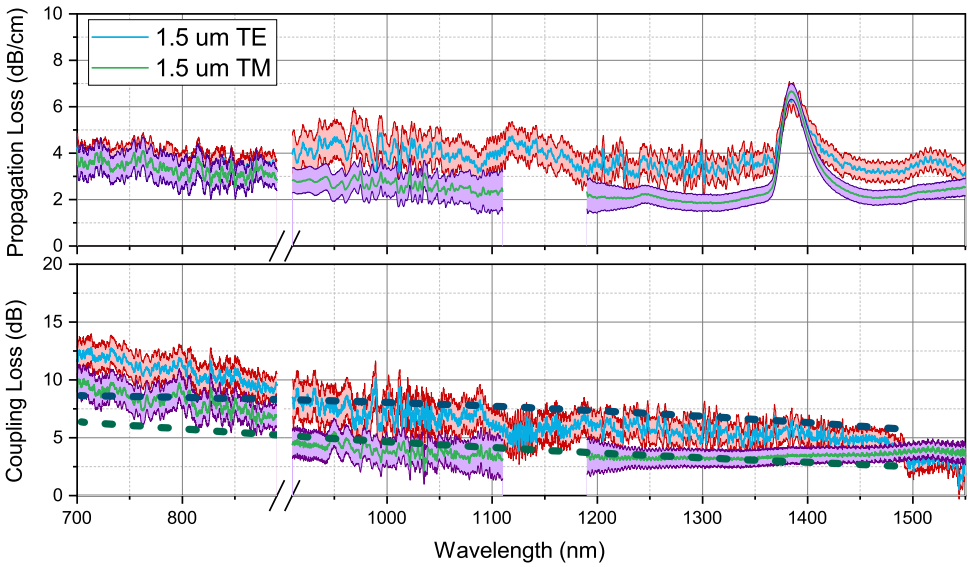

FIG. 6. Experimental coupling and propagation loss for both polarizations through a 1.5 μm waveguide on sample LZ, as well as the theoretical coupling loss (blue dashed line for the quasi-TE; green dashed line for the quasi-TM) for the lensed fibers used in this work. In both plots, TM data from 1110 nm to 1190 nm is not shown because of interference from mode-crossing minima centered at 1150 nm.

0.16 nm, which increases the effective coherence length to more than a millimeter. Thus, this "white-light spectroscopy" can interrogate complex interferometric structures, including *n*-stage lattice filters[22] and periodic Bragg gratings.[23] It is also suitable to test and refine components of ultrabroadband integrated systems, such as Raman and fluorescence sensors, on-chip signal interferometers, and arrayed waveguide gratings.

VII. CONCLUSIONS

We have described and demonstrated a powerful new *in situ* technique for ultrabroadband characterization of photonic waveguides: mode-crossing spectroscopy (MCS). MCS uses a simple blackbody source coupled to a single-mode fiber (spanning over an octave in spectral range) to observe the TM_{00}/TE_{x0} mode degeneracies in a waveguide. Though MCS requires a multimode, rectangular waveguide to observe the mode crossings, the material index or width uniformity information gleaned will apply to all waveguides on the sample, including narrower single-mode devices. In addition, waveguides with vertical symmetry permit much cleaner mode-crossing measurements and analysis. The core refractive index can be found with an error of ±0.5%, and lithography-based imperfections such as waveguide width variations can be quantified. In addition to material index, ultrabroadband propagation and coupling losses can be measured *in situ*, within an error of ±0.5 dB/cm and ±1.0 dB, respectively.

REFERENCES

[1]E. W. Ong, N. M. Fahrenkopf, and D. D. Coolbaugh, "SiNx bilayer grating coupler for photonic systems," OSA Continuum **1**, 13–25 (2018).

[2]S. A. Holmstrom, T. H. Stievater, D. A. Kozak, M. W. Pruessner, N. Tyndall, W. S. Rabinovich, R. A. McGill, and J. B. Khurgin, "Trace gas Raman spectroscopy using functionalized waveguides," Optica **3**, 891–896 (2016).

[3]A. Dhakal, P. Wuytens, A. Raza, N. Le Thomas, and R. Baets, "Silicon nitride background in nanophotonic waveguide enhanced Raman spectroscopy," Materials **10**, 140 (2017).

[4]N. F. Tyndall, T. H. Stievater, D. A. Kozak, K. Koo, R. A. McGill, M. W. Pruessner, W. S. Rabinovich, and S. A. Holmstrom, "Waveguide-enhanced Raman spectroscopy of trace chemical warfare agent simulants," Opt. Lett. **43**, 4803–4806 (2018).

[5]T. Wall, J. McMurray, G. Meena, V. Ganjalizadeh, H. Schmidt, and A. R. Hawkins, "Optofluidic lab-on-a-chip fluorescence sensor using integrated buried arrow (barrow) waveguides," Micromachines **8**, 252 (2017).

[6]D. Brooks and S. Ruschin, "Improved near-field method for refractive index measurement of optical waveguides," IEEE Photonics Technol. Lett. **8**, 254–256 (1996).

[7]S. T. Huntington, A. Roberts, K. A. Nugent, P. Mulvaney, and M. Bazylenko, "Fibre and waveguide refractive index measurements with AFM resolution," Jpn. J. Appl. Phys. **37**, 62 (1998).

[8]T.-N. Ding and E. Garmire, "Measuring refractive index and thickness of thin films: A new technique," Appl. Opt. **22**, 3177–3181 (1983).

[9]W.-S. Tsai, S.-Y. Ting, and P.-K. Wei, "Refractive index profiling of an optical waveguide from the determination of the effective index with measured differential fields," Opt. Express **20**, 26766–26777 (2012).

[10]J. Jágerská, N. L. Thomas, R. Houdré, J. Bolten, C. Moormann, T. Wahlbrink, J. Ctyroký, M. Waldow, and M. Först, "Dispersion properties of silicon nanophotonic waveguides investigated with fourier optics," Opt. Lett. **32**, 2723–2725 (2007).

[11]M. Moresco, M. Romagnoli, S. Boscolo, M. Midrio, M. Cherchi, E. S. Hosseini, D. Coolbaugh, M. R. Watts, and B. Dutt, "Method for characterization of Si waveguide propagation loss," Opt. Express **21**, 5391–5400 (2013).

[12]T. H. Stievater, M. W. Pruessner, D. Park, W. S. Rabinovich, R. A. McGill, D. A. Kozak, R. Furstenberg, S. A. Holmstrom, and J. B. Khurgin, "Trace gas absorption spectroscopy using functionalized microring resonators," Opt. Lett. **39**, 969–972 (2014).

[13]A. Trenti, M. Borghi, S. Biasi, M. Ghulinyan, F. Ramiro-Manzano, G. Pucker, and L. Pavesi, "Thermo-optic coefficient and nonlinear refractive index of silicon oxynitride waveguides," AIP Adv. **8**, 025311 (2018).

[14]M. A. Tran, T. Komljenovic, J. C. Hulme, M. L. Davenport, and J. E. Bowers, "A robust method for characterization of optical waveguides and couplers," IEEE Photonics Technol. Lett. **28**, 1517–1520 (2016).

[15]I. H. Malitson, "Interspecimen comparison of the refractive index of fused silica," J. Opt. Soc. Am. **55**, 1205–1209 (1965).

[16]H. J. Lee, C. H. Henry, K. J. Orlowsky, R. F. Kazarinov, and T. Y. Kometani, "Refractive-index dispersion of phosphosilicate glass, thermal oxide, and silicon nitride films on silicon," Appl. Opt. **27**, 4104–4109 (1988).

[17]S. V. Deshpande, E. Gulari, S. W. Brown, and S. C. Rand, "Optical properties of silicon nitride films deposited by hot filament chemical vapor deposition," J. Appl. Phys. **77**, 6534–6541 (1995).

[18]W. S. Rabinovich, P. G. Goetz, M. Pruessner, R. Mahon, M. S. Ferraro, D. Park, E. Fleet, and M. J. DePrenger, "Free space optical communication link using a silicon photonic optical phased array," Proc. SPIE **9354**, 93540B (2015).

[19]T. Miya, Y. Terunuma, T. Hosaka, and T. Miyashita, "Ultimate low-loss single-mode fibre at 1.55 μm," Electron. Lett. **15**, 106–108 (1979).

[20]C. H. Henry, R. F. Kazarinov, H. J. Lee, K. J. Orlowsky, and L. E. Katz, "Low loss Si_3N_4–SiO_2 optical waveguides on Si," Appl. Opt. **26**, 2621–2624 (1987).

[21]J. Wang, Y. Xuan, C. Lee, B. Niu, L. Liu, G. N. Liu, and M. Qi, "Low-loss and misalignment-tolerant fiber-to-chip edge coupler based on double-tip inverse tapers," in *2016 Optical Fiber Communications Conference and Exhibition (OFC)* (IEEE, 2016), pp. 1–3.

[22]N. F. Tyndall, T. H. Stievater, D. A. Kozak, M. W. Pruessner, S. A. Holmstrom, and W. S. Rabinovich, "Ultrabroadband lattice filters for integrated photonic spectroscopy and sensing," Opt. Eng. **57**, 1–5 (2018).

[23]P. T. Callahan, P. Purnawirman, T. N. Adam, G. Leake, D. Coolbaugh, M. R. Watts, and F. X. Kärtner, "Double-chirped Bragg gratings in a silicon nitride waveguide," in *2016 Conference on Lasers and Electro-Optics (CLEO)* (IEEE, 2016), pp. 1–2.